Progress In Electromagnetics Research, Vol. 169, 117–127, 2020

A Parameter-Free Calibration Process for a Scheimpflug LIDAR for Volumetric Profiling

Longqiang Luo, Xiang Chen, Zhanpeng Xu, Shuo Li, Yaoran Sun*, and Sailing He*

Abstract—Scheimpflug LIDAR has attracted considerable attention in the recent years, and has been widely applied in many fields due to its infinite depth of field. In this study, we reconstruct a series of formulas to demonstrate the Scheimpflug principles, with reference at the hinge point. These formulas based on directly measurable parameters are simple in form. Base on this, we report a new calibration for the Scheimpflug system, without measuring the instrument parameters. We also confirm that the result of calibration is accordance with the actual setting of the system. To take full advantage of the infinite depth of field of the Scheimpflug system, we have designed and carried out the system, combining with a rotary stage, to obtain the entire volumetric profile for a target of interest in a cycle rotation. To the best of our knowledge, this is the first time Scheimpflug system is utilized to perform a three-dimensional volumetric profile measurement.

1. INTRODUCTION

Dimensional metrology is always closely related to the use of light since ancient times. Nowadays, the demand of acquisition of three-dimensional (3D) information has arouse a considerable degree of interest in diverse applications, including navigation [1], industrial manufacturing [2], food science [3] and others [4]. Thus, many optical methods and techniques were developed with the advantage of high-accuracy, quick measurement and non-contacting against traditional mechanical probes [5].

The optical methods for depth ranging in 3D measurement can be divided into two categories. One is time-based, which calculates the distance between the object and observer by measuring the time of flight (TOF) that light travel between them. It can achieve a relatively large measuring range. However, it is confined to single point inspection, resulting in a time-consuming scanning procedure and a low lateral resolution. Another way is position-based, including stereo vision, laser range scanning, and structured illumination, etc. [6–13]. It scans a single line or a plane at a time and utilizes the principle of triangulation to derive the depth of those points. Due to the limited detection range determined by the depth of field (DOF), they are mostly applied to measure the depth profiles of surfaces with complex geometry shapes [14, 15].

An approach to infinite DOF is to adapt the Scheimpflug principles to set up the optics [16]. Briefly, the rule of Scheimpflug principles states that in a scenario where the object plane is tilted, sharp focus can be achieved by tilting the image sensor to a proper angle, where the image plane intersecting with the object plane and lens plane at the same point. Many scientific studies were benefit from it, such as particle image velocimetry [17–19], atmospheric aerosol monitoring [20–26] and fluorescence hyperspectral LIDAR [27–30]. Our previous study [31, 32] has shown the potential to measure the distance profiles by light-sheet based two-dimensional Scheimpflug LIDAR, which also demonstrates the ability of large measuring range.

Received 7 December 2020, Accepted 31 December 2020, Scheduled 31 December 2020
* Corresponding authors: Sailing He (sailing@jorcep.org), Yaoran Sun (sunoi@zju.edu.cn).
The authors are with the Centre for Optical and Electromagnetic Research, National Engineering Research Center for Optical Instruments, Zhejiang University, Hangzhou 310058, China.

Along with the application development of the Scheimpflug LIDAR, the analysis of the Scheimpflug rule also becomes important [33–36]. However, few study is aimed at ranging application. Thus, in this paper we establish a series of formulas in a simple form, with the reference at the Hinge points, to demonstrate the Scheimpflug rule clearly and simplify the calibration process. These formulas not only determine the axial distance but also lateral height, depicting the relationship between a spatial location and the corresponding pixel.

Apart from theoretical innovation, we also improve the application in the experiment. Notice that conventional acquisition systems for surface profiles can only measure from one side, and consequently multiple scanning paths for scanning data are required to obtain the entire 3D information, which makes the scanning time-consuming and less accurate [8, 37]. In this paper, we put the target object on a rotary stage, and use 2D Scheimpflug LIDAR to capture its profile of distance and height. This way we can collect and assemble the 2D information to obtain a 3D volumetric profile, while turning the target object a full cycle. Distinctive from a 2D surface profile scanner, this system can build a digital model for an entire object quickly and accurately, and may contribute greatly to intelligent manufacturing and reverse engineering, etc..

In the following part of this paper, we first discuss the geometrical relations for the Scheimpflug LIDAR. Then we adapt relations for calibration in Section 3. Finally, we demonstrate some experiments to evaluate the system. A brief conclusion summarizes our work in the end.

2. GEOMETRICAL RELATIONS IN SCHEIMPFLUG PRINCIPLE

Scheimpflug imaging system depicts a bi-axial optical scheme where the image plane and object plane are not parallel to the lens plane. Fig. 1(a) depicts the corresponding relation of the three planes, viewing from the direction parallel to them. The green line represents the object plane, which is tilted to the primary optics axis with an angle of φ, and the corresponding image plane is on the left side of the lens, indicated by the red line. On the meridian plane, we use two yellow dashed lines to label the locations of focus planes. In order to fully demonstrate the space geometry of Scheimpflug, we can also view the schematic diagram from another direction, as shown in Fig. 1(b). As indicated by the coordinate axes in the upper right corner, the viewing directions for Fig. 1(a) and Fig. 1(b) are along the z and y directions, respectively. Thus, a line (e.g., the red line) in Fig. 1(a) is actually an intersection line of a plane with the xy plane, and thus can correspond to a plane (e.g., the red plane/region) in Fig. 1(b). The projections of the image and object planes (which are represented by lines in Fig. 1(a)) on the xz plane are denoted as a red region and a green region, respectively, in Fig. 1(b). Meanwhile,

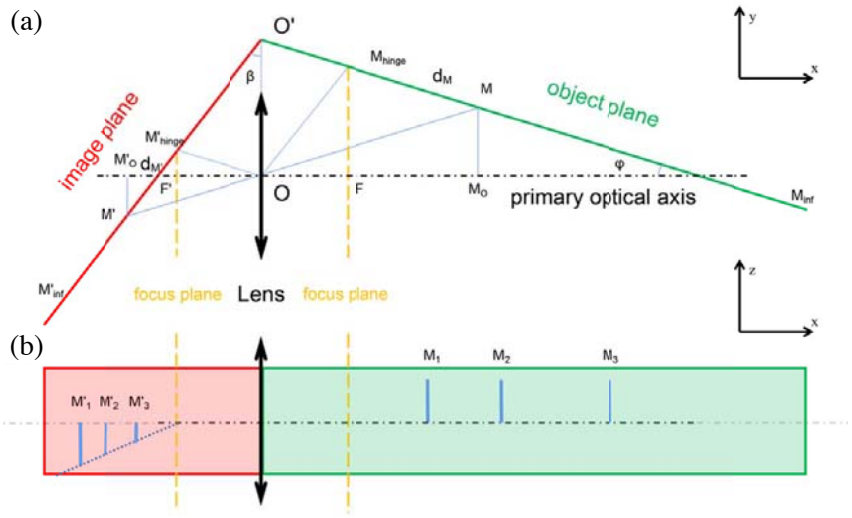

Figure 1. (a) Schematic diagram for Scheimpflug geometrical optics on the meridian plane; (b) Projection view of the image plane and object plane.

a vertical line in Fig. 1(b) corresponds to a point in Fig. 1(a). The projection of the intersection of the focus plane and object plane on the meridian plane (i.e., the xy plane) is denoted as the hinge point (M_{hinge}) in Fig. 1(a). Similarly, there is another hinge point on the image plane. Note that there is a more important point, Scheimpflug point O', which is the intersection of the object plane, the lens plane and the meridian plane.

For any point M on the object plane beyond the focus plane, we can derive the location of its corresponding image point from the following formulas.

$$x_M \cdot x_{M'} = -f^2 \tag{1}$$

$$m = \frac{y_{M'}}{y_M} = \frac{x_{M'}}{f} = -\frac{f}{x_M} \tag{2}$$

where f is the focal length. Eqs. (1) and (2) are derived from the Newtonian optics directly, where x_M is the distance from point M to the focus plane, i.e., $|FM_o|$; $x_{M'}$ is the distance from the image point M' to the image focus plane, i.e., $|F'M'_o|$; y_M and $y_{M'}$ are the lateral distances, and equal to lengths $|MM_o|$ and $|M'M'_o|$, respectively; m represents the lateral magnification. Furthermore, as point M was on the object plane (line), objective lateral length y_M and objective axial distance x_M should satisfy the following equation

$$y_M = d - (x_M + f) \cdot \tan\varphi \tag{3}$$

where d is the distance of the Scheimpflug point to the lens center.

Considering the corresponding image point M', and the angle between $M'O'$ and the lens plane is denoted by $\beta_{M'}$. Based on the geometry relations, its tangent can be expressed as follows:

$$\tan\angle M'O'O = \tan\beta_{M'} = \frac{-x_{M'} + f}{d - y_{M'}} \tag{4}$$

Using Eqs. (1)–(3), we can simplify the above equation through the following process:

$$\begin{aligned}\tan\beta_{M'} &= \frac{f^2/x_M + f}{d + f \cdot y_M/x_M} = \frac{f \cdot (f/x_M + 1)}{d + f \cdot (d - (x_M + f) \cdot \tan\varphi)/x_M} \\ &= \frac{f \cdot (f/x_M + 1)}{(d - f \cdot \tan\varphi) \cdot (f/x_M + 1)} = \frac{f}{d - f \cdot \tan\varphi}\end{aligned} \tag{5}$$

As expected, $\beta_{M'}$ is irrelevant to x_M. That is to say, for any point in the object plane, $\beta_{M'}$ is a constant determined by d, f and φ. Viewing from the perspective of imaging, we can conclude that the corresponding image plane is flat and intersects with the lens plane at the Scheimpflug point with a angle of β, as labeled in Fig. 1(a).

Let's analyze one special point on the object plane, M_{hinge}. M_{hinge} is also on the focus plane, its corresponding image point (M'_{inf}) will locate at the infinity. Thus, OM'_{inf} is paralleled to $O'M'_{inf}$. Furthermore, OM_{hinge} and OM'_{inf} are collinear, since O is the center of the lens. Therefore, we can conclude that $O'M'_{inf}$ is paralleled to OM_{hinge}. We can also draw the same conclusion mathematically. Since the lateral distance of M_{hinge} can be derived from Eq. (3), i.e., $y(M_{hinge}) = d - f \cdot \tan\varphi$, we have

$$\tan\angle O'OM_{hinge} = (x(M_{hinge}) + f)/y(M_{hinge}) = \frac{f}{d - f \cdot \tan\varphi} = \tan\beta \tag{6}$$

Eq. (6) demonstrates the particularity of the hinge point. Geometrically, the image plane is parallel to the line connecting the hinge point and the center of the lens, which is also called the hinge plane. This provide optical engineers with a simple geometric method to determine and locate the image plane. Similarly, the hinge plane on the image side is parallel to the object plane.

In order to fully clarify the rule of imaging, we should observe the Scheimpflug imaging system from a different perspective — a plane perpendicular to Fig. 1(a), as shown in Fig. 1(b). Notice that the object plane and image plane are obliquely projected (not parallel) to this figure.

For any line perpendicular to the meridian plane, with a height of z_M and a distance x_M to the focus plane, the height of its imaging line $z_{M'}$ can be expressed as follows:

$$z_{M'} = z_M \cdot m \tag{7}$$

where m represents the radial magnification (the same as that in Eq. (2)). Hence the image ratio of $z_{M'}$ and $x_{M'}$ can be expressed as

$$\frac{z_{M'}}{x_{M'}} = \frac{z_M \cdot m}{-f^2/x_M} = \frac{z_M \cdot (-f/x_M)}{-f^2/x_M} = \frac{z_M}{f} \tag{8}$$

We can see that this ratio is irrelevant to x_M. Furthermore, if the object height is fixed, this image ratio remains invariable at different objective distances. As we can see from Fig. 1(b), there are three lines of the same height arranged on the object plane, labeled as M_1, M_2 and M_3. Their image lines are located at M_1', M_2' and M_3', respectively. We draw a dashed line connecting the endpoints of them, and the line will reach the hinge point. Hence, for a line on the object plane parallel to the projection of the primary optical axis, the corresponding image line is straight and will reach M'_{hinge}.

Equation (8) indicates a simple way to locate the hinge point on the image side, i.e., to compute the image intersect of two lines parallel with the projection of the primary axis on the object plane. Once the hinge point is determined, the distance on the object side can be easily computed by Eqs. (1) and (2).

This section has demonstrated the Scheimpflug imaging system from the perspective of geometry, which will be fully utilized in the following calibration process.

3. SYSTEM SET-UP AND CALIBRATION

In the previous section, we have given some mathematics analysis to describe an ideal situation with sufficient and accuracy parameters. However, it is not easy to measuring these parameters in the experiment and quite often the result obtained is inaccurate. Hence, we set up the experiment to calibration the scenario (where we do not need to know any parameters in advance) and determine the corresponding relationship between the pixel and location.

Figure 2(a) presents a photo of the Scheimpflug module, which consists of a consumer camera lens (Canon EFS 18-55), a camera (ZWO ASI174MM), and a blue line laser module. As the Scheimpflug rule requires, the image plane must intersect with the lens plane and object plane at the same point. In practice, the object plane and image plane are equivalent to the laser illumination plane and camera plane, respectively. Hence we placed the camera on a kinematic mount and tuned the camera slanted to the lens, to make the image of the laser line very clear in the whole measuring range. At this point the camera (i.e., image) plane and the illumination (i.e., object) plane are conjugated, satisfying the Scheimpflug principles. As we labeled in Fig. 2(a), the image plane (red line), the lens plane (black line), and the object plane (blue line) joined at one point.

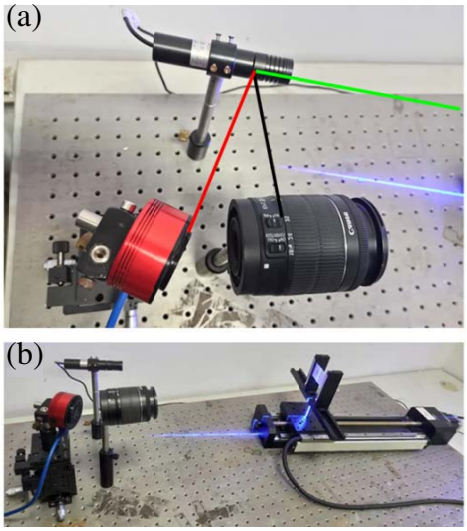

Figure 2. (a) A photo of the Scheimpflug module; (b) A scenario during the calibration process.

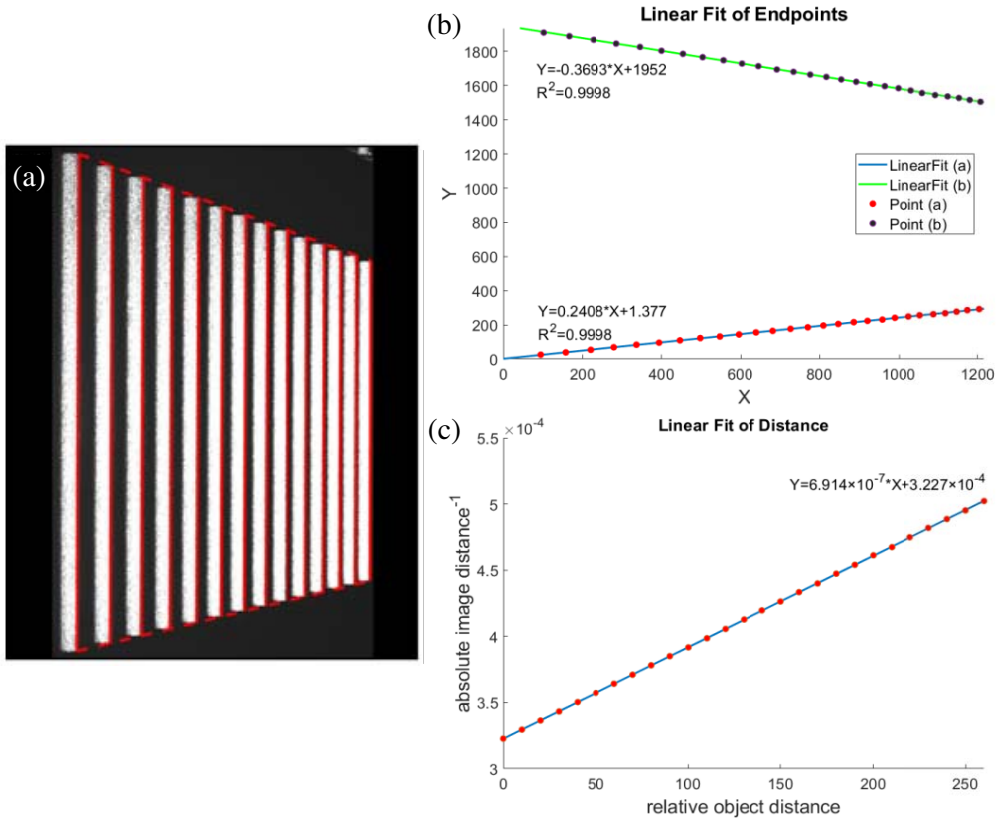

Figure 3. (a) Superimposed image with the object at different distances; (b) Linear fitting of the endpoints; (c) Linear fitting of the curve for the reciprocal of the image distance as the object distance increases.

The next step is to quantify the image pixel with the spatial distance and height. Hence, we placed a metal plate on a translation stage (Zolix KA100) moving along the laser output direction, as shown Fig. 2(b). Then, we took a sequence of 27 images of the metal plate on the stage continuously, as it moving backward with each step of 20 mm. We superimposed some of these images and exhibited them in Fig. 3(a). Since the shining width of the output laser beam (light-sheet) will reduce the distance resolution, we extracted its right boundary and marked with a red line.

As we can see from Fig. 3(a), the red lines shift from left to right, as the metal plate moving away from the lens. Furthermore, its height decreases as well as the gap between them. This is in accordance with the general imaging laws, i.e., the image size decreases as the object distance increases. Now we can pay attention to the endpoints of each light bar (red line), corresponding to the edge of the metal plate, which moves in parallel with the primary optical axis. Our previous study in Section 2.2 has demonstrated that the hinge point on the image side locates at the image intersect of two lines parallel with the projection of the primary axis (see Fig. 1(b)). In previous study image thinning techniques were usually adopted to exact the center of the light bar. However, our system has a larger image magnification, and thus the size of the light bar in the image is wider, covering a considerably large area, which is usually of different shape. The reason we extracted the side boundary instead of the center in the image processing algorithm is to improve the measurement accuracy.

Thus, we plot two lines to linearly fit the top and bottom endpoints separately in Fig. 3(b). The fitted equations are $y = -0.3693 \times x + 1952$ and $y = 0.2048 \times x + 1.377$. The absolute values of their first order fitting coefficients are not equal, which means that the hinge point is not on the middle line of the camera. More importantly, the R-square values are 0.9998 for both, indicating a pretty good linearity (this also proves the new calibration theory demonstrated in Section 2). To determine the pixel location of the hinge point, we calculate the intersect of the two fitted lines, and the result is

$M'_{hinge} = (3196, 771)$.

On the other hand, it is much more important and difficult to determine the hinge point on the object plane as compared to that on the image side, since it is impossible to construct a paralleled line on the image plane. Nevertheless, in this study we explored a new method to solve the problem. As illustrated by Eq. (1), the product of $x_{M'}$ and x_M is a constant. Simultaneously, $x_{M'}$ is proportional to the distance $d_{M'}$ between the image location and image hinge point, i.e., $x_{M'} \propto d_{M'}$. Similarly, $x_M \propto d_M$. Hence the product of d_M and $d_{M'}$ is a constant. In our experiment, we can express $d_{M'}$ in unit of pixels and d_M in unit of millimeter as follows:

$$d_{M'} = px(M') - px(M'_{hinge}) = px(M') - 3196 \tag{9}$$

$$d_M = d - d_0 \tag{10}$$

where $px(M')$ is the pixel index of the center point of each light bar in x direction; $px(M'_{hinge})$ is the x pixel index of the image hinge point; d_0 is the distance from the object hinge point to the starting point of the translational movement, and d is the relative distance of motion. Since the product of d_M and $d_{M'}$ is a constant, we can fit it linearly for the relation between d and $1/d_{M'}$, both of which are already known in the calibration process.

The fitting result shows a high linearity, as depicted in Fig. 3(c). To evaluate the reference distance d_0, we compute the x-axial intercept of the fitted line, and the result is -466. That means the hinge point is 466 mm away from the starting point, opposite to the moving direction.

So far, we have come up with a particular calibration approach based on a linear fitting of the endpoints, to determine the hinge point on the image side and object side. Base on that, we can establish a relationship between the pixel index and spatial location. First, in order to calibrate the distance, we compute the coefficient $F^2 = (px(M') - px(M_{hinge})) \times (d - d_0)$ for each image. Statistically, we found that the mean value $\mathrm{E}(F^2) = -1.446 \times 10^6$ with a standard deviation $\sigma(F^2) = 581$. As we can see, F^2 is almost invariable, which is in good agreement with our theory. Hence we can determine the calibration expression of distance as

$$d = F^2 / \left(px(M') - px(M'_{hinge})\right) + d_0 = -1.446 \times 10^6 / (x - 3196) + (-466) \tag{11}$$

From the above expression, we can also know how the distance resolution varies with x pixel index and is 0.22 mm at the center of the image. However, the actual resolution greatly depends on the quality of image captured in the experiment.

Then, according to Eq. (8), we know that the height of the target is proportional to the image height $py(M')$ and inversely proportional to $d_{M'}$ (see Fig. 1(b)). Furthermore, in the height calibration processing, a metal plate acts as a reference, with a height of 89 mm. Hence, we can obtain the following calibration formula for the height:

$$h = C \times \left(\mathrm{p}y(M') - py(M'_{hinge})\right) / \left(px(M') - px(M'_{hinge})\right) = 145.91 \times (y - 771)/(x - 3196) \tag{12}$$

where C is the coefficient computed from the data we measured in the calibration process. The standard deviation of C is 0.2014, which is quite small compared with mean value $E(C) = 145.91$. From Eq. (12), we see that the height corresponding to one pixel in the y direction is about 0.05 mm.

As mentioned in the introduction section, the Scheimpflug system is of infinite DOF. However, the detection range is determined by the size of the image sensor in practice. According to Eq. (11) we know that the detection range in depth is 276.7 mm. On the other hand, the detection ranges in height are different at near end and far end, which are 88 mm and 143 mm, respectively, according to Eq. (12).

So far, we have demonstrated a progressive calibration approach, requiring no parameter of the system set-up, but can achieve fitting with good linearity and calibrating pixel by pixel with small standard deviation for the characterizing coefficients. Meanwhile, we also want to verify the result with actual parameter of the system. Thus, we measured the following parameters: the focal length of the lens ($f = 55$ mm), the distance between the Scheimpflug point and lens center ($l = 150$ mm), the angle of the laser illumination plane and lens plane ($\tan\varphi = 0.2075$), pixel size of the camera ($w_0 = 5.86\,\mu$m), the angel of the camera plane to the lens plane ($\tan\beta = 0.3969$). Then, we take the first pair of endpoints in the image sequence, with $px(M') = 97$ and $d(M) = 0$. Hence, we can calculate that

$$x_{M'} = (px(M') - px(M'_{hinge})) \times \sin\beta \times w_0 = -6.71\,\mathrm{mm} \tag{13}$$

$$x_M = (d(M) - d(M_{hinge})) \times \cos\varphi = 456.3\,\mathrm{mm} \tag{14}$$

Substituting them into Eq. (1), we can obtain $f = 55.33\,\text{mm}$, which is very close to the actual focal length. This means that the progressive calibration approach is well matched with the physical truth.

4. EXPERIMENT AND APPLICATION

In order to fully demonstrate the capacity of the system, we carry out some tests and discuss the result of them in this section. Two target objects tested in our experiment are a metal cylinder and a pile of sundries. Different from the push-broom and whisk-broom scanning procedures, we place the laser and camera on the ground, and put the target object on a rotary stage. The scanning procedure is achieved by rotating the object, so that we can obtain the volumetric profiles of the entire object.

Therefore, the first thing is to place the rotary stage (Zolix RAuK-100) with its axis on the illumination plane, and place a blocker vertically at its center, as shown in Fig. 4(a). Then we take an image with the camera, to find out the distance of the rotary axis. The image was shown in Fig. 4(b), the x pixel index is 965, and thus the relative distance is 179.45 mm, according to calibration formula (11).

Then we put a metal cylinder on the stage concentrically, and illuminate it with a line laser, as shown in Fig. 5(a). While the cylinder rotates one cycle on the stage with steps of 0.5 degree, we snap its image frame by frame, and Fig. 5(b) exhibits one frame in the image sequence. Employing some image processing technique, we can characterize the edge of the pattern, which is marked with red pixels. Then we convert the marked pixels into spatial points with height and distance, according to calibration Eqs. (8), (9). In order to depict the volumetric profiles of the cylinder, we need to calculate the relative distance to the rotary axis, and transform the coordinate based on the relative distance and current rotation angle. Finally, we plot the 3D point cloud in Fig. 5(c), where we label the point

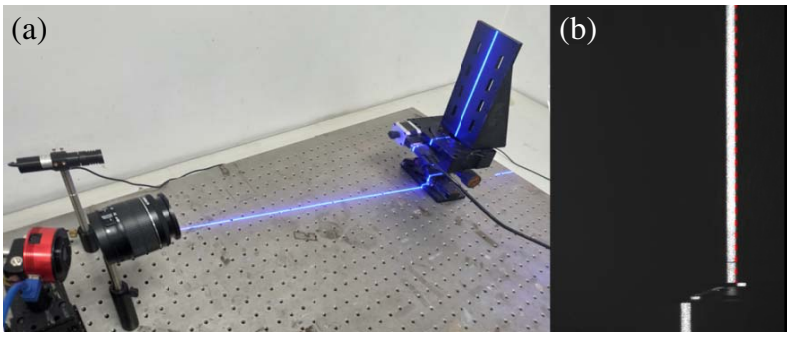

Figure 4. (a) Set-up with the Scheimpflug module and the rotary stage; (b) Image of the block.

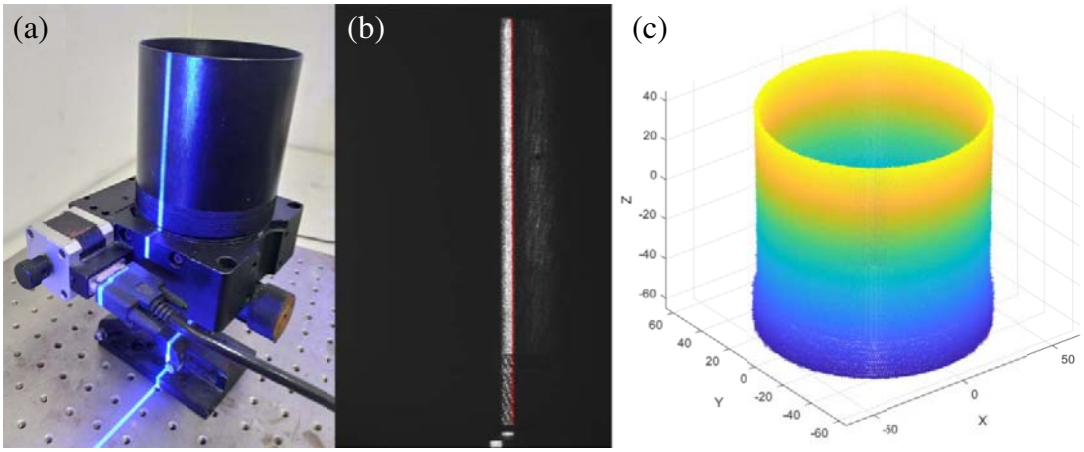

Figure 5. (a) Photo of a cylinder; (b) One snapshot image; (c) 3D point cloud model.

of different height with different color.

From Fig. 5(c), we can estimate the height and diameter of the cylinder to be 108 mm and 100 mm, respectively. The result accords with the actual size measured manually, and that means the three-dimensional volumetric output is reliable. However, we notice that the bottom part of the cylinder, looks thicker graphically than the other parts of the cylinder. This is due to the knurling on the cylinder bottom, which makes it hard to exact the edge in the image processing. As we can see in Fig. 5(b), the bottom part of the marked red line has some zigzag feature.

Next we try to capture the volumetric profile of a target of complex structure. This time we use a pile of sundries, from the bottom to the top, including a metal ring, a cardboard box and a gummed tape, as shown by the photo of Fig. 6(a). The metal ring at the bottom is totally shielded by the box, from the perspective of the photo. We measured the size of these objects. The outer diameter of the metal ring and tape are 69 mm and 120 mm, approximately. The dimension of the cardboard box is 252 mm × 165 mm × 62 mm.

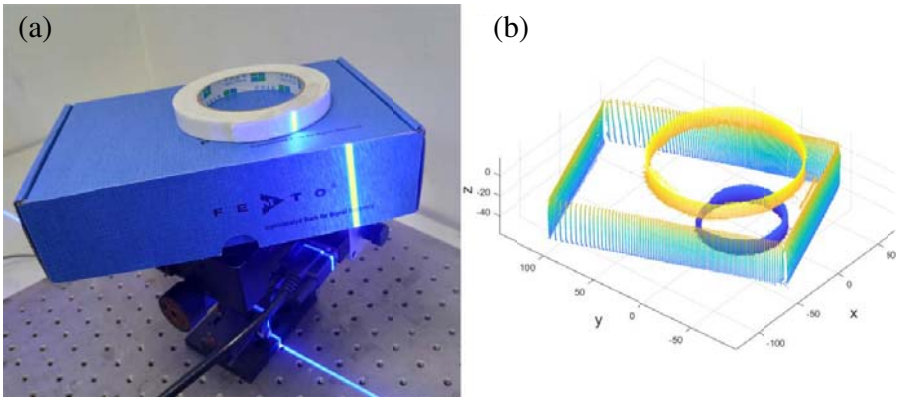

Figure 6. (a) Photo of the target; (b) 3D point cloud model.

The structure of the target is complex with discrete planes, which can only be measured with a device with a large depth of field, such as the Scheimpflug system. With the intention to verify the robustness of the system, we place them asymmetrically and unbalanced.

In order to display clearly the result of every rotational scan, we set the step of the rotary stage to 1 degree, so we capture 360 images in total. The corresponding result is shown in Fig. 6(b). We can see a sequence of vertical lines clearly around the perimeter of the box, i.e., the result of each scan. They become intensive near the rotary axis, and become sparse when far away from the rotary axis.

Choosing a proper region of interest (ROI), as shown by the red box in Fig. 7(a), we can analyze the small metal ring separately, which is enlarged in Fig. 7(b). Due to the knurled surface, the accuracy of the measurement is limited. This is the same as all other active 3D illumination measurement, such as the structured light scan method. The difficulty is in image edge exaction. We also notice that some points of the top part were missing near sides, which is shielded by the box from the view of camera. Nevertheless, the result is still convincing. Let's take a look of top view, as shown in Fig. 7(c). The red dots represent the computed location of the points and the black circles give the shape. We can find the diameter of the circle is about 69 mm, which demonstrates a relatively high precision. The mean error is about 2 mm, due to the coarseness of the knurled surface.

We also choose one side of the cardboard box for numerical analysis, as shown in Fig. 8. The box in the inset encircles the points extracted. We try to fit the point cloud with a flat surface, taking x and z as independent variables, and y as a dependent variable. Hence, we obtain $y = -67.24 + 0.3902x + 0.03029z$, and draw a semitransparent plane with black dashed line edges to visualize the flat plane. The root mean squared error of the fitting is 0.1775 mm, which is less than the distance corresponding to one pixel. This indicates the error in edge exaction is about one pixel. However, this only represents a relative precision, but not absolute accuracy. Furthermore, the coefficient of z is close to zero, indicating the plane is nearly vertical.

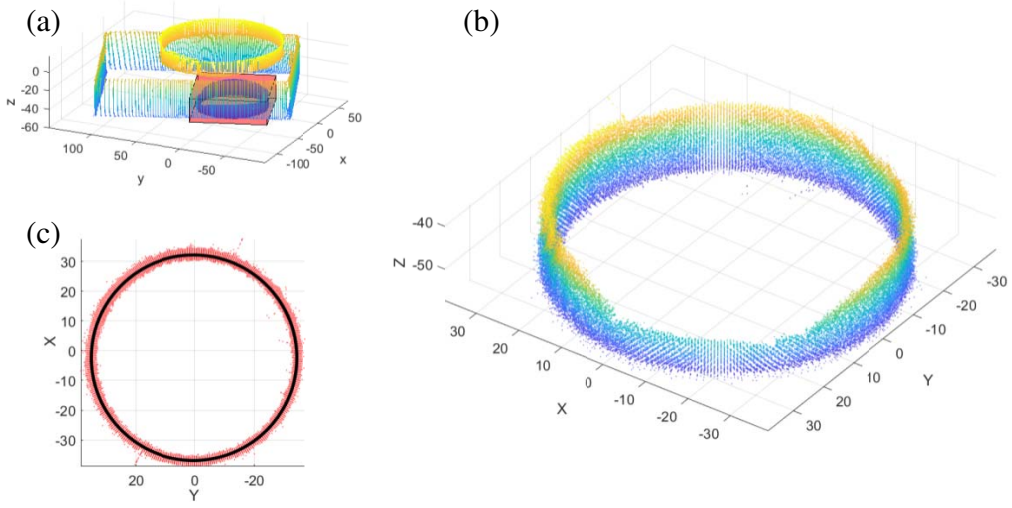

Figure 7. (a) Region of interest; (b) 3D point cloud chosen; (c) View from the x-y plane.

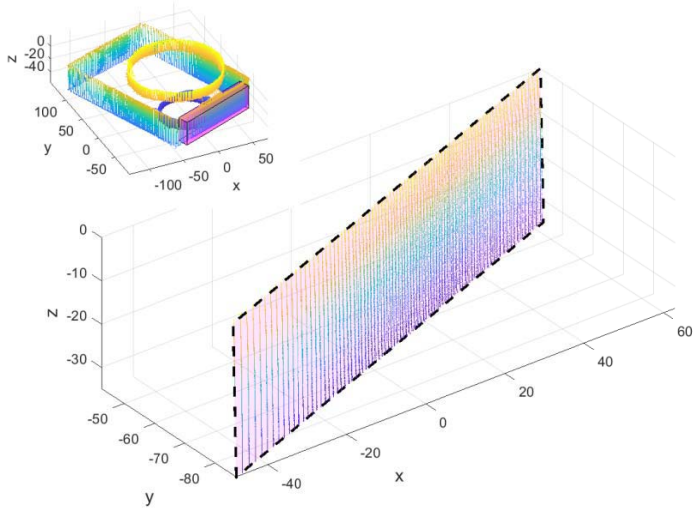

Figure 8. Planar fitting of one side of the cardboard box.

5. CONCLUSIONS

In this paper, we have analyzed the geometrical relations of the Scheimpflug principle from the perspective of Hinge point, originated from the Newtonian lens equation. Compared with the Gaussian form of the lens equation, Newtonian equation is algebraically simpler by setting the distance reference at the focal points. Furthermore, the lateral magnification m can also be expressed in the Newtonian form. We have shown that the image of a line parallel to the projection of the primary optical plane on the object side is straight and will pass through the hinge point on the image side. Based on the above conclusion, we have proposed a convenient and precise calibration method, without measuring the instrument parameters, but by geometrically computing the images of the references at different distances. The calibration result agrees well with the actual parameters.

The Scheimpflug system has the advantage of infinite depth of field, but can measure only a line at a time. Conventional techniques for surface profile measurement (e.g., structured illumination) has a larger width of field, but limited in the distance range. To fully exploit the advantages of the Scheimpflug system and measure the volumetric profile of an object, we put an object on a rotary stage. As the

target rotates with the stage, we capture its line shape to composite a volumetric profile. With this method, we can obtain the entire volumetric profile of a complex target very quickly.

We have carried out two experiments to demonstrate our system, and analyzed the precision and accuracy numerically. The measuring errors for a smooth cardboard and knurled metal are about 0.17 mm and 2 mm, respectively. We believe that our 3D volumetric profile inspection technique based on the Scheimpflug system has great potential for industrial utilization in the near future.

ACKNOWLEDGMENT

This work was supported by the National Key Research and Development Program of China (No. 2018YFC1407503), Key Research and Development Program of Zhejiang Province (2021C03178), the Fundamental Research Funds for the Central Universities (Zhejiang University NGICS Platform), the Ningbo Science and Technology Project (No. 2020G012), the National Natural Science Foundation of China (62007029, 11621101), the Science and Technology Development Plan Project of Changshu (No. CS201806), and the Ningbo Science and Technology Project (No. 2018B10093).

REFERENCES

1. Fu, G., A. Menciassi, and P. Dario, "Development of a low-cost active 3D triangulation laser scanner for indoor navigation of miniature mobile robots," *Robotics and Autonomous Systems*, Vol. 60, 1317–1326, 2012.
2. Schwenke, H., et al., "Optical methods for dimensional metrology in production engineering," *CIRP Anmanuf. Technol.*, Vol. 51, 685–699, 2002
3. Lu, Y. and R. Lu, "Structured-illumination reflectance imaging coupled with phase analysis techniques for surface profiling of apples," *Journal of Food Engineering*, Vol. 232, 11–20, 2018.
4. Sansoni, G., M. Trebeschi, and F. Docchio, "State-of-the-art and applications of 3D imaging sensors in industry, cultural heritage, medicine, and criminal investigation," *Sensors*, Vol. 9, 568–601, 2009.
5. Nadolny, K. and W. Kaplonek, "Analysis of flatness deviations for austenitic stainless steel workpieces after efficient surface machining," *Measurement Science Review*, Vol. 1, 204–212, 2014.
6. Ye, J., et al., "3D reconstruction of line-structured light based on binocular vision calibration rotary axis," *Applied Optics*, Vol. 5, 8272–8278, 2020.
7. Wang, J. and Y. Yang, "High-speed three-dimensional measurement technique for object surface with a large range of reflectivity variations," *Applied Optics*, Vol. 57, 9172–9182, 2018.
8. Schlarp, J., E. Csencsics, and G. Schitter, "Optical scanning of laser line sensors for 3D imaging," *Applied Optics*, Vol. 57, 5242–5248, 2018.
9. Lilienblum, E. and A. Al-Hamadi, "A structured light approach for 3-D surface reconstruction with a stereo line-scan system," *IEEE Trans. Instrum. Meas.*, Vol. 64, 1266–1274, 2015.
10. Yang, Y., et al., "3D color reconstruction based on underwater RGB laser line scanning system," *Optik*, Vol. 125, 6074–6077, 2014.
11. Cai, F., et al., "High-resolution mobile bio-microscope with smartphone telephoto camera lens," *Optik*, Vol. 20, 164449, 2020.
12. Cai, F., et al., "Handheld four-dimensional optical sensor," *Optik*, Vol. 20, 164001, 2020.
13. Xu, Z., et al., "Light-sheet microscopy for surface topography measurements and quantitative analysis," *Sensors*, Vol. 20, 284210, 2020.
14. Blais, F., "Review of 20 years of range sensor development," *Journal of Electronic Imaging*, Vol. 13, 231–243, 2004.
15. Lin, H., et al., "Review and comparison of high-dynamic range three-dimensional shape measurement techniques," *Journal of Sensors*, Vol. 2017, 957685, 2017.
16. Brydegaard, M., et al., "The Scheimpflug lidar method," *SPIE Lidar Remote Sensing for Environmental Monitoring*, Vol. 10406, 104060I, 2017.

17. Prasad, A. K., "Stereoscopic particle image velocimetry," *Experimentsin Fluids*, Vol. 29, 103–116, 2000.
18. Zang, W. J. and A. K. Prasad, "Performance evaluation of a Scheimpflug stereocamera for particle image velocimetry," *Applied Optics*, Vol. 36, 8738–8744, 1997.
19. Prasad, A. K. and K. Jensen, "Scheimpflug stereocamera for particle image velocimetry in liquid flows," *Applied Optics*, Vol. 34, 7092–7099, 1995.
20. Kong, Z., et al., "Three-wavelength polarization Scheimpflug lidar system developed for remote sensing of atmospheric aerosols," *Applied Optics*, Vol. 5, 8612–8621, 2019.
21. Larsson, J., et al., "Atmospheric CO2 sensing using Scheimpflug-lidar based on a 1.57-μm fiber source," *Optics Express*, Vol. 27, 17348–17358, 2019.
22. Sun, G., et al., "Small-scale Scheimpflug lidar for aerosol extinction coefficient and vertical atmospheric transmittance detection," *Optics Express*, Vol. 26, 7423–7436, 2018.
23. Mei, L., P. Guan, and Z. Kong, "Remote sensing of atmospheric NO2 by employing the continuous-wave differential absorption lidar technique," *Optics Express*, Vol. 25, A953–A962, 2017.
24. Mei, L. and P. Guan, "Development of an atmospheric polarization Scheimpflug lidar system based on a time-division multiplexing scheme," *Optics Letters*, Vol. 42, 3562–3565, 2017.
25. Mei, L., et al., "Atmospheric extinction coefficient retrieval and validation for the single-band Mie-scattering Scheimpflug lidar technique," *Optics Express*, Vol. 25, A628–A638, 2017.
26. Mei, L. and M. Brydegaard, "Atmospheric aerosol monitoring by an elastic Scheimpflug lidar system," *Optics Express*, Vol. 23, 1613–1628, 2015.
27. Lin, H., Y. Zhang, and L. Mei, "Fluorescence Scheimpflug LiDAR developed for the three-dimension profiling of plants," *Optics Express*, Vol. 28, 9269–9279, 2020.
28. Wang, X., et al., "Drone-based area scanning of vegetation fluorescence height profiles using a miniaturized hyperspectral lidar system," *Applied Physics B — Lasers and Optics*, Vol. 12, 20711, 2018.
29. Zhao, G., et al., "Inelastic hyperspectral lidar for profiling aquatic ecosystems," *Laser & Photonics Reviews*, Vol. 10, 807–813, 2016.
30. Gao, F., et al., "Oil pollution discrimination by an inelastic hyperspectral Scheimpflug lidar system," *Optics Express*, Vol. 25, 25515–25522, 2017
31. Chen, K., et al., "Overwater light-sheet Scheimpflug lidar system for an underwater three-dimensional profile bathymetry," *Applied Optics*, Vol. 58, 7643–7648, 2019.
32. Gao, F., et al., "Light-sheet based two-dimensional Scheimpflug lidar system for profile measurements," *Optics Express*, Vol. 26, 27179–27188, 2018.
33. Peng, J., et al., "Distortion correction for microscopic fringe projection system with Scheimpflug telecentric lens," *Applied Optics*, Vol. 54, 10055–10062, 2015.
34. Yin, X., et al., "Analysis and simplification of lens distortion model for the Scheimpflug imaging system calibration," *Optics Communications*, Vol. 43, 380–384, 2019.
35. Sun, C., et al., "Review of calibration methods for Scheimpflug camera," *Journalof Sensors*, Vol. 2018, 3901431, 2018.
36. Miks, A., J. Novak, and P. Novak, "Analysis of imaging for laser triangulation sensors under Scheimpflug rule," *Optics Express*, Vol. 21, 18225–18235, 2013.
37. Li, J., et al., "Calibration of a multiple axes 3-D laser scanning system consisting of robot, portable laser scanner and turntable," *Optik*, Vol. 122, 324–329, 2011.